Journal Pre-proof

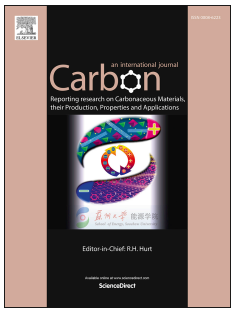

Carbon catalysts derived from ZIF-8: Joule heating vs. furnace heating

Leo Lai, Songbo Ye, Fangzhou Liu, Fangxin She, Justin Prabowo, Jiaxiang Chen, Yeyu Deng, Hao Li, Li Wei, Yuan Chen

PII: S0008-6223(24)01201-6

DOI: https://doi.org/10.1016/j.carbon.2024.119982

Reference: CARBON 119982

To appear in: *Carbon*

Received Date: 28 September 2024

Revised Date: 15 December 2024

Accepted Date: 31 December 2024

Please cite this article as: L. Lai, S. Ye, F. Liu, F. She, J. Prabowo, J. Chen, Y. Deng, H. Li, L. Wei, Y. Chen, Carbon catalysts derived from ZIF-8: Joule heating vs. furnace heating, *Carbon*, https://doi.org/10.1016/j.carbon.2024.119982.

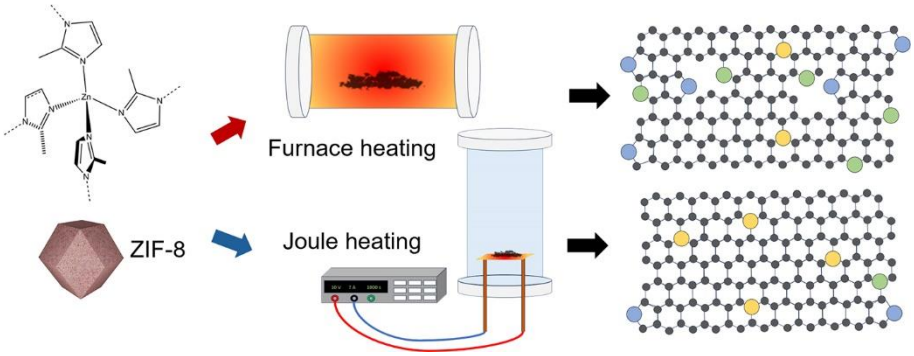

Carbon catalysts derived from ZIF-8: Joule heating vs. furnace heating

Leo Lai [1], Songbo Ye [2], Fangzhou Liu [1], Fangxin She [1], Justin Prabowo [1], Jiaxiang Chen [1], Yeyu Deng [1], Hao Li [2*], Li Wei [1*], Yuan Chen [1*]

1. School of Chemical and Biomolecule Engineering, The University of Sydney, Sydney, New South Wales, Australia, 2006
2. Advanced Institute for Materials Research (WPI-AIMR), Tohoku University, Sendai, Japan, 980-8577

***Corresponding authors.**

Email addresses: li.hao.b8@tohoku.ac.jp (H. Li); l.wei@sydney.edu.au (L. Wei); yuan.chen@sydney.edu.au (Y. Chen)

Abstract

Carbon catalysts synthesized using metal-organic frameworks are promising for various applications. However, their carbonization process is still poorly understood. Here, we systematically studied carbon catalysts derived from ZIF-8 using the standard furnace heating (FH) and a new Joule heating (JH) method. The JH method produced carbon catalysts with significantly higher catalytic activity for oxygen reduction reaction (ORR). Statistical analysis based on the correlation between different structural features and performance descriptors of the nitrogen-doped carbon catalysts identifies the carbon atoms bonded to graphitic-N as their ORR active sites. Surprisingly, the abundance of N species in JH-derived carbon catalysts is only half that of FH-derived carbon catalysts, indicating lower active site density. However, further evaluation revealed that the intrinsic activity of individual active sites in the JH-derived carbon catalysts with a higher graphitization degree is more than twice that of the FH-derived carbon catalysts. The enhanced intrinsic catalytic activity of these active sites outpaces the reduction in their numbers, resulting in overall better activity. Theoretical calculations indicate that the rate-determining step on these active sites is the conversion of OH* to H_2O with a lower energy barrier. Our findings reveal the synergistic effect of heteroatom coordination environment and graphitization degree of carbon structures in determining the catalytic performance of carbon catalysts while featuring JH as a new approach to realize high-performance carbon catalysts through simultaneously regulating these properties.

Keywords: carbon catalyst; Joule heating; carbonization; oxygen reduction reaction; metal-organic frameworks

1. Introduction

Carbon materials are promising catalysts for various chemical processes, such as petroleum refineries, biomass transformation, and fuel cells [1-5]. They offer unique advantages, such as tunable surface chemistry, high specific surface area, enhanced mass transport via porous structure, and chemical stability [6]. However, their broad adoption is constrained by the lack of a clear understanding of their catalytically active sites and technical difficulty in precisely regulating their structures [7-9]. A milestone in carbon catalyst studies was the discovery of N-doped carbon nanotubes (CNTs) as metal-free cathode catalysts for oxygen reduction reaction (ORR) in hydrogen fuel cells by Dai et al. [6]. N in N-doped carbon materials can adopt different atomic structures, such as pyridinic, pyrrolic, and graphitic N, which leads to debates on the actual structure of catalytically active sites. Nakamura et al. designed a series of N-doped oriented pyrolytic graphite (HOPG), and pyridinic-N-dominated HOPG was discovered to be more active than graphitic-N-dominated HOPG [10]. Further studies proposed carbon atoms connected to pyrrolic N, graphitic N, or structural defects of carbon materials as catalytically active sites [11-14]. We notice that different conclusions are drawn when using various types of precursors: ones with intrinsic graphitic structures, such as HOPG, CNTs, carbon black, and graphene vs. others without existing graphitic structures, such as highly defective carbon materials produced by pyrolysis of organic precursors. The correlation between the graphitization degree of carbon substrates and doped heteroatoms and their resulting catalytic activity is not clearly understood.

A common precursor in recent carbon catalyst synthesis is metal-organic-frameworks (MOFs) or covalent-organic-frameworks (COFs) [6, 15-17]. They offer tunable and controllable chemical composition, highly porous structures, and large specific surface areas. These organic precursors are commonly thermally treated in an inert or slightly reducing protective gas atmosphere to be carbonized with doped heteroatoms. Previous studies have demonstrated that a range of factors, including heating temperature [18-20], heating temperature ramping speed [18, 21, 22], gas environment [23], and the size of MOF/COF particles [24], can significantly impact the catalytic activity of resulting carbon

catalysts. Recent studies have also utilized in-situ characterization tools to track the removal of heteroatoms and the formation of different structural and morphological features during the thermal treatment of these catalysts [21, 22]. These findings underscore the complexity of carbon catalyst synthesis from MOFs/COFs and the need for better understandings.

In the commonly used furnace heating method, MOFs/COFs receive thermal radiation from heated furnace walls with relatively low heat fluxes (e.g., <1 MW m^{-2}) and slow heating ramping speed (e.g., <100 °C min^{-1}). Unlike carbon catalysts derived from originally graphitized carbon materials (e.g., HOPG, CNTs, or graphene), a low graphitization degree of carbon substrates from MOFs/COFs would compromise their electrical conductivity. In contrast, excessive thermal treatments (e.g., prolonged thermal treatments at high temperatures) would collapse their porous structures. Furthermore, heating conditions influence the mass content vs. the phase distribution of heteroatoms in carbon substrates. Recent studies have suggested that thermal treatment via several new heating methods, such as laser irradiation, microwave heating, or direct Joule heating (JH), may overcome the technical limits of standard thermal treatment methods, offering higher heat fluxes and ultrafast heating rates [25-27]. It is intriguing to explore the effect of JH on the structure and catalytic properties of carbon catalysts.

Here, we systematically studied carbon catalysts derived from a commonly used MOF precursor (i.e., ZIF-8) by furnace heating (FH) and JH methods. We first compared their electrocatalytic properties for ORR, which show significant variations correlated with their heating methods and durations. Next, we tried but failed to directly correlate their electrocatalytic properties with their critical structural characteristics, including graphitization, N heteroatoms, surface area, and pore structures. Further, Spearman's correlation coefficient analysis was conducted to identify an interplay between graphitization degree and graphitic N species of carbon substrates. Based on the statistical analysis, carbon atoms bonded to graphitic N species were identified as catalytically active sites. Density function theory (DFT) calculations further confirmed the intrinsic catalytic activity of different potential active sites and supported experimental results.

2. Methodology/Experimental

2.1 *Chemicals and materials*

Carbon cloth (W0S1011) was obtained from Suzhou Sinero Technology Co., Ltd.. Nafion™ 117 solution (5 wt%), ethanol (anhydrous) 2-propanol (IPA, 99.5%), potassium hydroxide (semiconductor grade), and ZIF-8 (Basolite® Z1200) were from Sigma-Aldrich. Argon (Ar, grade 5.0) and oxygen (O_2, grade 5.0) were from BOC Australia. Deionized water (DI H_2O) was obtained from a water purification system (Merck MilliQ). The structure of ZIF-8 was confirmed by X-ray diffraction (XRD) (Fig. S1 in Supplementary Information (SI)).

2.2 *Carbon catalyst synthesis by JH*

The carbon cloth was first cut into 1 × 4 cm^2 slices and heated to 1000 °C for 3 h under Ar flow to improve thermal stability. The carbon cloth slices were further rinsed with ethanol three times before dried in a vacuum oven. In a typical synthesis, 100 mg of ZIF-8 was dispersed in 20 mL IPA. 2 mL of the ZIF dispersion was sprayed to the center region of the treated carbon cloth (1 × 3 cm^2). A DC power supply (VOLTEQ HY30100EX) delivered an electrical current through the carbon cloth loaded with ZIF-8 to generate heat. A programmable oscillator (2280S-60-3, Keithley) was used to control the heating internals (see a photo of the JH reactor in Fig. S2 in SI). The carbon cloth surface temperature was increased to 900 °C in about 9 seconds in Ar and then retained at the temperature for varied times from 10 to 180 min. The resulting carbon catalysts were denoted as JH-*x*, where *x* refers to their heating time at 900 ºC.

2.3 *Carbon catalyst synthesis by FH*

In a typical synthesis, 50 mg of ZIF-8 was loaded on a ceramic boat and placed in a tube furnace. A thermal couple was attached to the ceramic boat to monitor its temperature. The temperature was increased to 900 °C at a rising rate of 5 °C min^{-1} in Ar and then retained at the temperature for varied times from 30 to 300. The resulting carbon catalysts were denoted as FH-*x*, where *x* refers to their heating time at 900 ºC.

2.4 *Electrochemical tests*

The electrocatalytic properties of the carbon catalysts for ORR were characterized using the standard three-electrode test. 3 mg of carbon catalysts were sonicated in a mixture of 534 μL of IPA, 60 μL of DI H_2O water, and 6 μL of Nafion^{TM} 117 solution for 1 hour at room temperature to prepare homogenous catalyst ink. Then, 8 μL of catalyst ink was drop-casted on pre-polished glassy carbon surfaces of rotating ring-disk electrodes (RRDE, E6R1, Pine Research) with a catalyst mass loading of 0.2 mg cm^{-2}. Subsequently, all electrochemical tests were conducted using an electrochemical workstation (CHI, 760E) in 0.1 M KOH electrolyte (pH = 12.6). A Hg/HgO (0.1 M KOH) was used as the reference electrode, and a graphite rod (6.4 mm diameter, AFCTR3B, Pine Research) was used as the counter electrode. All potentials were calibrated to a reversible hydrogen electrode (RHE).

Before electrochemical tests, 20 cyclic voltammetry (CV) scans were performed in Ar-purged electrolytes at a scan rate of 100 mV s^{-1} between 0.1 to 1 V_{RHE} to stabilize the catalysts. Linear sweep voltammetry (LSV) polarization curves were obtained in Ar- or O_2-saturated electrolytes at a scan rate of 5 mV s^{-1} with an electrode rotation speed of 1600 rpm to collect disk currents (i_{disk}). The Pt-ring electrode was biased at 1.2 V_{RHE} to collect ring currents (i_{ring}). The Faradaic efficiency related to H_2O_2 production ($FE_{H_2O_2}$) and the corresponding electron transfer number (n) were calculated using the following equations:

$$FE_{H_2O_2} = 100 \times \frac{i_{ring}/N}{|i_{disk}|} \quad (1)$$

$$n = 4 \times \frac{|i_{disk}|}{|i_{disk}| + i_{ring}/N} \quad (2)$$

where $N = 0.25$ is the calibrated electron collection efficiency of the RRDE electrodes used.

The ORR kinetic current density (j_k) was calculated using the Koutecký-Levich equation:

$$\frac{1}{j} = \frac{1}{j_d} + \frac{1}{j_k} = \frac{1}{0.62nFC_o{D_o}^{2/3}v^{-1/6}w^{1/2}} + \frac{1}{j_k} \quad (3)$$

where j and j_d is the overall and diffusive current density, n is the electron transfer number, F is the Faraday constant (96485 C mol^{-1}), C_o is the O_2 concentration in electrolytes (1.2×10^{-3} M), D_o is the

O_2 diffusion coefficient (1.9×10^{-5} cm^2 s^{-1}), v is the kinetic viscosity of water, which is 0.01 cm^2 s^{-1}. The turnover frequency (TOF) of catalytically active sites was calculated by assuming three carbon atoms bonded to an N atom as active sites using the following equation:

$$TOF = \frac{j_k}{n \cdot 3 \cdot 0.2 \cdot m_N / M_w} \quad (4)$$

where n is the electron transfer number, 3 is the number of carbon atoms bonded to an N atom, 0.2 is the carbon catalyst mass loading in mg cm^{-2}, m_N is the mass abundance of different types of N species in catalysts, and M_w is the molecular weight of N (14 g mol^{-1}).

The electrochemically active surface area (ECSA) of catalysts was obtained from their CV curves collected in an Ar-purged electrolyte at the scan rates from 5 to 40 mV s^{-1}. Their double-layer capacitance (C_{dl}) was calculated by the linear fitting of the currents to the scan rates, and the ECSA was calculated by:

$$\text{ECSA} = C_{dl}/C_s \quad (5)$$

where C_s is the specific capacitance of graphitic materials (0.02 mF cm^{-2}).

2.5 *Physicochemical characterization*

The carbon catalyst surface morphology was first examined by scanning electron microscopy (SEM) using a Zeiss Sigma HD VP microscope. The atomic structures were analyzed by transmission electron microscopy (TEM) using a FEI SPECTRA microscope. Specific surface area (SSA) and pore structures were quantified by N_2 physisorption using a Quantachrome Autosorb iQ gas adsorption analyzer. The SSA and pore size distribution were calculated using the Brunauer-Emmett-Teller (BET) and the non-local density functional theory (NL-DFT) methods, respectively. Their chemical compositions were investigated by four methods. First, thermalgravimetric analysis (TGA) was conducted using a thermalgravimetric analyzer (TA Instruments Q500) under an airflow with a temperature increase from 25 to 900 ºC at a ramping rate of 15 ºC min^{-1}. Second, Raman spectra were collected using a Renishaw InVia Reflex spectrometer with a 532 nm laser. Third, surface chemical composition was analyzed by X-ray photoelectron spectroscopy (XPS) using a ThermoScientific K-

Alpha+ spectrometer equipped with an Al-Kα source (1486.8eV). Last, the elemental distribution was also mapped by energy-dispersive X-ray spectroscopy (EDS) using scanning transmission electron microscopy (STEM-EDX).

2.6 *Computation methods*

DFT calculations were performed using the Vienna *Ab initio* Simulation Package (VASP). The Kohn−Sham wave functions expanded in a plane-wave basis set, and the generalized gradient approximation method with the PBE (Perdew-Burke-Ernzerhof) functional were used to describe the valence electrons and electron correlations, respectively. In contrast, the core electrons were treated using the projector augmented-wave method [28-31]. The atomistic models were fully relaxed to allow geometry optimization until all the forces were lower than 0.05 eV $Å^{-1}$. The Brillouin zone was sampled by the 1 × 3 × 1 Γ-point. The 4-electron ORR pathway was considered based on the computational hydrogen electrode method [32, 33].

2.7 *Zinc-air battery (ZAB) assembly and tests*

The catalyst ink for ZAB assembly was prepared by dispersing 10 mg of carbon catalysts in a mixture of 8.91 mL IPA, 0.98 mL DI H_2O, and 100 μL of Nafion^{TM} 117 solution by 1-hour sonication. The ZAB cathodes were prepared by drop-casting 0.785 mL of the catalyst ink onto a carbon cloth with a circular active area (d = 1cm) and a mass loading of 1 mg cm^{-2}. Zn plates (100 μm in thickness) were sanded with 300, 800, 1000, 1500, and 2000 grit in sequence and used as ZAB anodes. An aqueous solution of 6 M KOH and 0.2 M $Zn(OAc)_2$ was used as the electrolyte.

All ZAB tests were conducted using a Metrohm Autolab PGSTAT302N workstation. The ZAB was activated by open circuit potential (OCP) scans until the variation was within the range of $\pm 10^{-6}$ V. The specific discharge capacitance of the cell was determined by a galvanostatic scan at 20 mA cm^{-2}. The specific discharge capacitance was calculated by:

$$C = j \times A/m_{Zn} \quad (6)$$

where C is the specific capacitance (mAh g^{-1}), A is the active area (0.785 cm^{-2}), and m_{Zn} is the mass of the reacted Zn plate.

The polarization curves were collected by galvanostatic scan from 0–500 mA cm^{-2}, and the power density was calculated by:

$$P = j \times V \quad (7)$$

where V is the potential measured, and j is the current density.

The galvanostatic discharge curves were collected using galvanostatic scans at different current densities at 10 mA cm^{-2}, 20 mA cm^{-2}, 50 mA cm^{-2}, 20 mA cm^{-2} and 10 mA cm^{-2}. Each specified current density was held for 1800 s before proceeding to the next one.

3. Results and Discussion

3.1 *Synthesis of carbon catalysts by JH and FH methods*

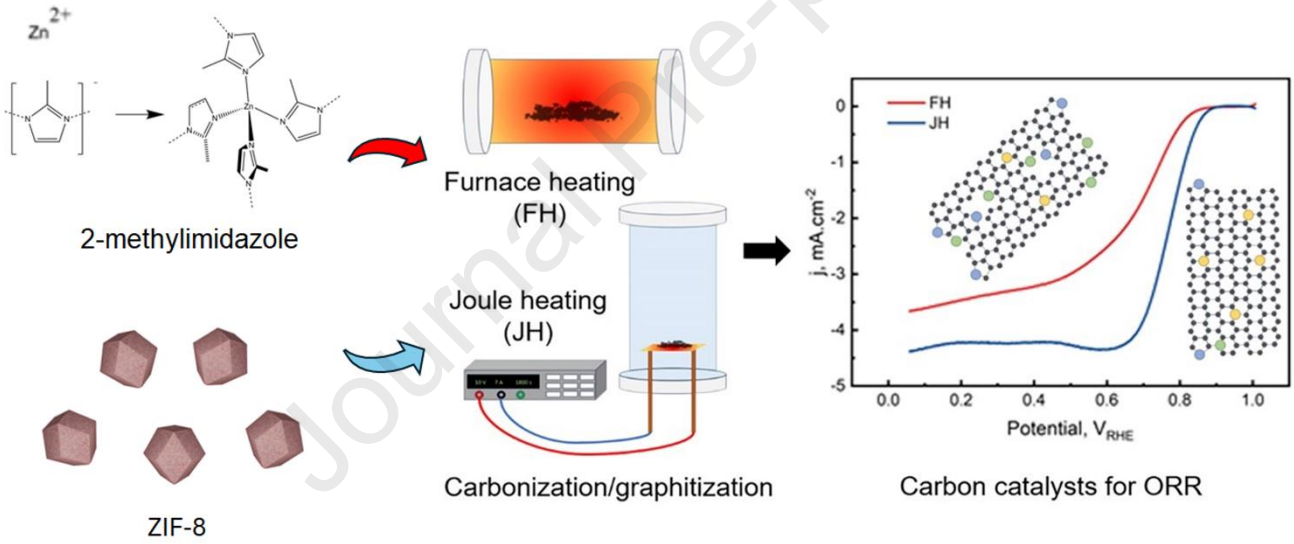

Fig. 1. Schematic illustration of the synthesis of carbon catalysts for ORR from ZIF-8 by the JH and FH methods.

Fig. 1 illustrates the synthesis of carbon catalysts for ORR by JH and FH thermal treatment methods using ZIF-8 as the precursor. The transformation of organic ZIF-8 into carbon catalysts involves a fast thermal decomposition to release volatile elements (i.e., H and N from imidazolate and Zn ions) at relatively lower temperatures and then a slow graphitization of resulting carbon materials at higher temperatures. We first performed TGA of ZIF-8 in N_2 from 25 to 900 °C with a 5 °C min^{-1} ramping

rate and stayed at 900 °C for 1 hour to examine the ZIF-8 transformation. The TGA profile (Fig. S3 in SI) is consistent with those reported in previous studies [34]. The thermal decomposition started slightly below 400 °C, and the fast mass loss ends around 600 °C. Only 32 wt.% of the original mass was left after staying at 900 °C for 1 hour.

We noticed three factors that affect the experimental result consistency of the JH method. First, the uniformity of ZIF-8 particle distribution on carbon cloth is essential. The non-uniform distribution of ZIF-8 particles would cause significant variation in the resulting carbon catalyst properties. Thus, we used an air spray method to coat ZIF-8 particles dispersed in IPA on carbon cloth to yield a uniform ZIF-8 particle coating with a mass loading of 3.3 mg cm^{-2}. Second, accurately monitoring and controlling the temperature of the Joule-heated carbon film is essential. This was achieved using a pyrometer. As shown in Fig. S2c in SI, the carbon cloth temperature shows minor fluctuations of ± 10 °C at 900 ºC. We also confirmed the temperatures of the heated carbon film in the JH and the ceramic boat used in FH are the same. Third, the JH method can enable much faster heat ramping rates than the FH method. Different heat ramping rates affect the thermal decomposition of ZIF-8. We fixed the ramping rate used in the JH method at ~90 °C s^{-1}, about 540 times faster than that in the FH method at 0.167 °C s^{-1}.

Since 900 °C has also been reported as the optimum temperature to synthesize carbon catalysts from ZIF-8 in several previous studies [35-37], we selected 900 °C for JH and FH thermal treatments. We varied their time at 900 °C to achieve different degrees of graphitization. The resulting carbon catalysts are denoted as JH-*x* (*x* from 10 to 180 min) and FH-*x* (*x* from 30 to 300 min), respectively.

3.2 *Basic physiochemical properties*

The representative SEM images of carbon catalysts (FH-240 and JH-120) are displayed in Fig. 2a–b. They show shrinkage and deformation of carbon particles compared to pristine ZIF-8 particles (Fig. S4 in SI). The original morphological features of ZIF-8 particles are preserved in FH-240 despite being obtained with a more prolonged thermal treatment at 900 ºC. Carbon particles in JH-120 appear to be

merged into a continuous surface, which may result from the rapid temperature ramping of the JH method. Their EDX elemental mapping results in Fig. 2**Error! Reference source not found.**c–d indicate that N, O, and C are uniformly distributed in FH-240 and JH-120; uniform elemental distribution was also observed in all other carbon catalysts. The total N content is 7.4 and 4.9 wt% for FH-240 and JH-120, respectively. It is also interesting to note that FH-240 contains more N than JH-120, even with the much longer thermal treatment. TEM images in Fig. 2e–f show that the amorphous carbon phase dominates both catalysts. Some graphitic layers could be observed near the edge of JH-120 (Fig. 2g), whereas few could be observed in FH-240 (Fig. 2h).

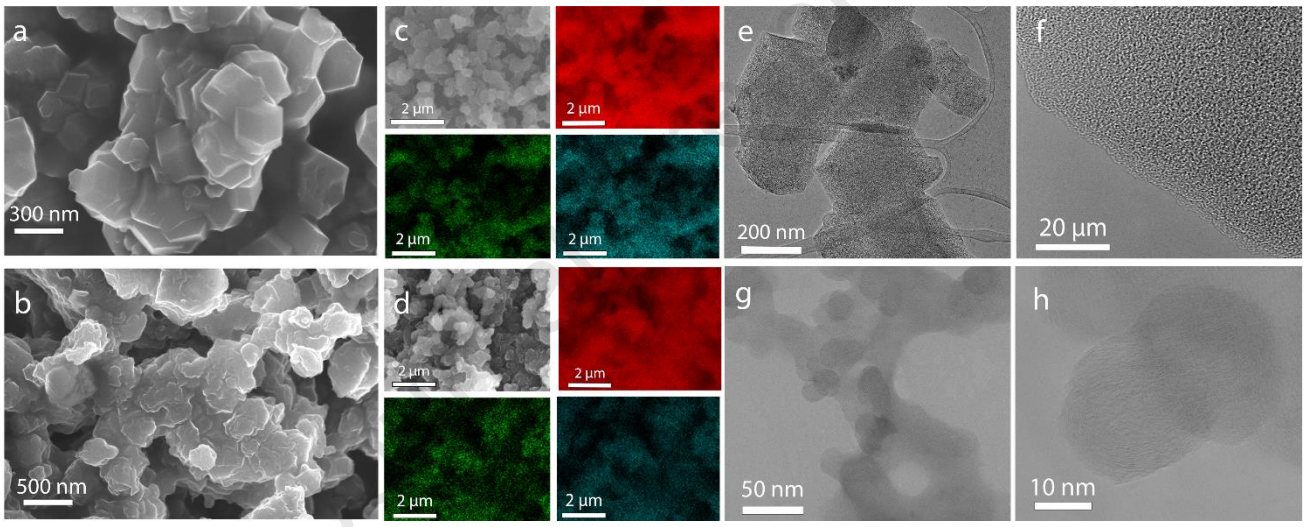

Fig. 2. Electron microscope images of FH-240 and JH-120, SEM images of (a) FH-240 and (b) JH-120, and the corresponding SEM C, N, and O EDS scans of (c) FH-240 and (d) JH-120, TEM images (e-f) FH-240 and (g-h) JH-120.

3.3 *Electrocatalytic properties of carbon catalysts*

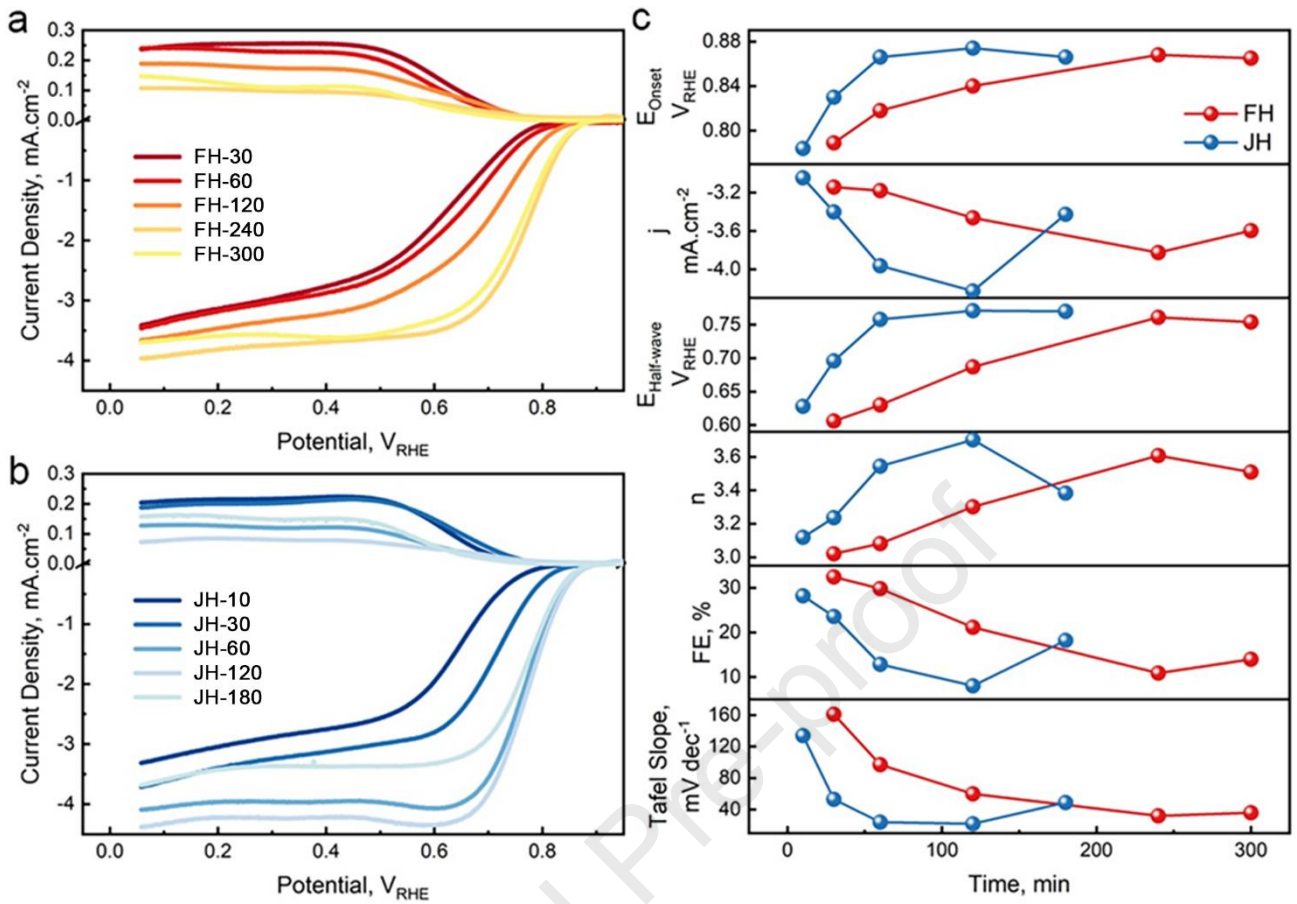

Fig. 3. ORR electrocatalytic properties of carbon catalysts. LSV curves of carbon catalysts synthesized by (a) the JH method and (b) the FH method. (c) Comparison of electrocatalytic performance descriptors of carbon catalysts plotted against their graphitization time at 900 ºC. From top to bottom: onset potential (E_{Onset}) at 0.1 mA cm^{-2}, limiting current (j) at V_{RHE} = 0.1 V, half-wave potential ($E_{Half\text{-}wave}$), electron transfer number (n), $FE_{H_2O_2}$, and Tafel slope.

Next, we compared the electrocatalytic properties of the carbon catalysts for ORR in 0.1 M KOH electrolyte (summarized in Table S1-2 in SI). The electrode fabrication and test methods are described in the experimental section. Their LSV curves are compared. Fig. 3a and 3b show LSV curves of FH-*x* and JH-*x*, respectively. Several electrocatalytic performance descriptors were extracted from LSV curves in Fig. 3a and 3b and compared in Fig. 3c vs. their graphitization time at 900 ºC. With the

increased graphitization time at 900 ºC from 30 to 240 min, the onset potential (E_{Onset}) of FH-*x* shifts from 0.789 to 0.868 V, indicating improved catalytic activity. When the graphitization time is further increased to 300 min, E_{Onset} slightly drops to 0.865 V, showing a catalytic activity decline. A similar trend was observed for the other two catalytic activity descriptors: limiting current (*j*) at 0.1 V and half-wave potential ($E_{Half\text{-}wave}$). *j* changes from -3.140 to -3.826 mA cm^{-2} and then back to -3.595 mA cm^{-2}, while $E_{Half\text{-}wave}$ shifts from 0.606 to 0.761 V and then returns to 0.754 V. The catalytic selectivity between 4-electron and 2-electron pathways also correlates similarly with the graphitization time. The electron transfer number (*n*) of FH-*x* increases from 3.02 to 3.61 when the graphitization time extends from 10 to 240 min and then slightly drops to 3.51, which indicates that the selectivity towards the 4-electron pathway increases first and then slightly drops. Correspondingly, the selectivity toward H_2O_2 production via the 2-electron pathway ($FE_{H_2O_2}$) has the same trend. It drops from 48.1 to 19.3% first and then slightly increases to 24.1%. Furthermore, the ORR kinetics were quantified using Tafel plots (Fig. S5 in SI). The Tafel slope drops from 97 to 58 mV dec^{-1} when the graphitization time increases from 10 to 240 min, indicating that FH-*x* undergone more prolonged graphitization treatment catalyzes faster reactions. Then, the Tafel slope increases to 63 mV dec^{-1}, indicating a slight drop in reaction kinetics. Overall, these results suggest sufficient graphitization time for FH-*x* is essential to improve their catalytic activity, selectivity toward the 4-electron pathway, and reaction kinetics. The optimum graphitization time at 900 ºC is around 240 min. Excessive graphitization time beyond 240 min would lead to a decline in catalytic performance.

The carbon catalysts (JH-*x*) synthesized by the JH method show a similar trend with two differences. With the change of graphitization time from 10 to 180 min at 900 ºC, the electrocatalytic performance descriptors of JH-*x* show similar changing trends as those of FH-*x*. Fig. 3c shows that E_{Onset} shifts from 0.784 to 0.874 V and returns to 0.866 V. *j* changes from -3.043 to -4.227 mA cm^{-2} and returns to -3.425 mA cm^{-2}. $E_{Half\text{-}wave}$ shifts from 0.628 to 0.771 V, then returns to 0.770 V. *n* increases from 3.12 to 3.70 and then drops to 3.38. $FE_{H_2O_2}$ drops from 43.3 to 14.6% first and then slightly increases to

30.4%. The Tafel slope drops from 120 to 56 mV dec^{-1} and increases to 59 mV dec^{-1}. The first difference is that the graphitization time to reach the peak electrocatalytic performance is much shorter at 120 min. Second, the peak catalytic performance of JH-*120* is also better than that of FH-240 in all six performance descriptors. In particular, the JH-120's j of -4.227 mA cm^{-2}, $FE_{H_2O_2}$ of 14.6%, and the Tafel slope of 56 mV dec^{-1} are much better than those of FH-*240* at -3.826 mA cm^{-2}, 19.3%, and 58 mV dec^{-1}, respectively.

3.4 *Graphitization, N heteroatoms, surface area, and pore structures*

Achieving high electrocatalytic performance for ORR in carbon catalysts requires a high electrical conductivity to enable efficient electron transfer, abundant catalytic active sites to catalyze ORR, and excellent accessibility to allow efficient mass transfer of gases, ions, and reaction intermediates. We reason that the difference between FH-*x* and JH-*x* carbon catalysts likely results from their different graphitization, N heteroatoms, surface area, and pore structures, which determine their electrical conductivity, the abundance of catalytic active sites, and mass transfer. Thus, we carried out various characterizations to quantify these properties of FH-*x* and JH-*x* carbon catalysts.

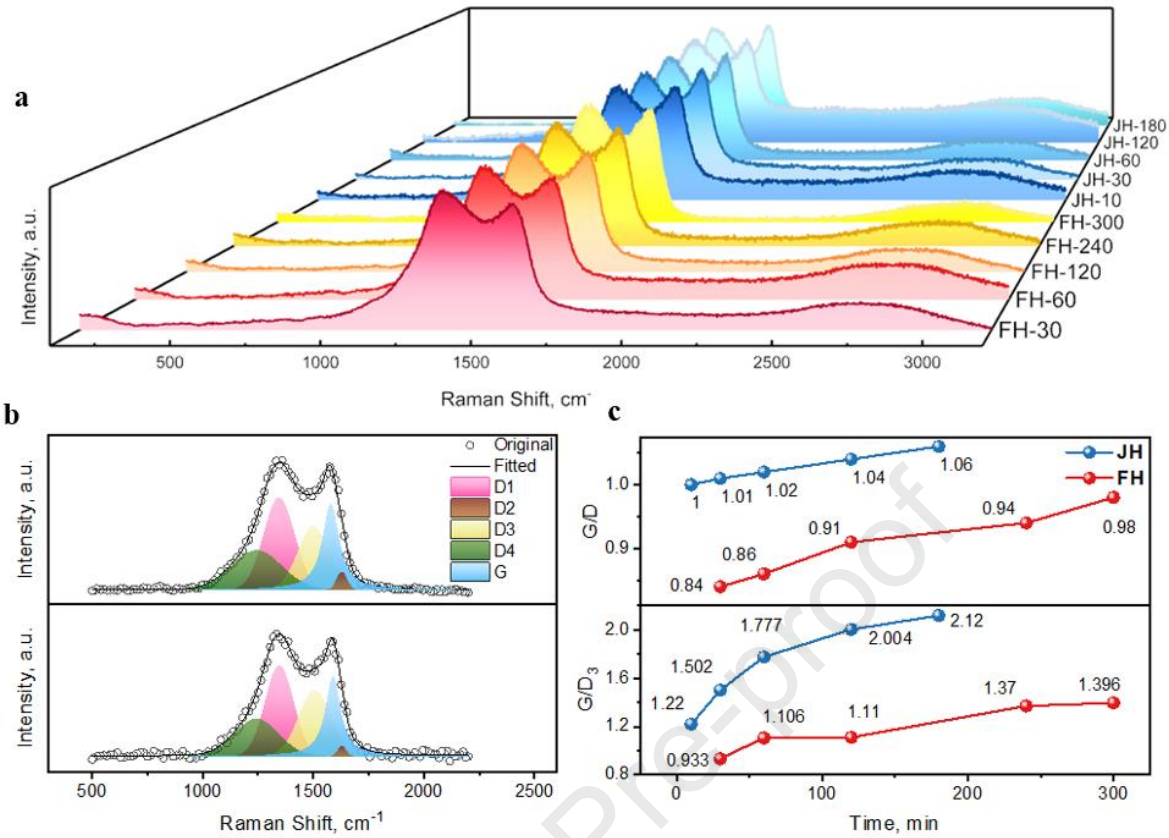

Fig. 4. Raman spectra of carbon catalysts, (a) Raman curves of all carbon catalysts, (b) the representative deconvolution of D and G bands of FH-*240* and JH-*120*, (c) G/D and G/D_3 ratio of carbon catalysts extracted from (a) plotted against their graphitization time at 900 ºC.

We first quantified the graphitization of FH-*x* and JH-*x* using Raman spectroscopy, shown in Fig. 4a. Their D (1350 cm^{-1}) and G (1580 cm^{-1}) band peaks are broad, indicating a lack of long-distance graphitic features and the existence of large amounts of structural defects [38]. Fig. 4c displays the continuous rise of G/D ratios (calculated based on the intensity of D and G band peaks) in FH-*x* and JH-*x* with the extension of graphitization time, indicating continuous improvement in their graphitization. JH-*x* has much higher G/D ratios than FH-*x,* even with a much shorter graphitization time. For example, The G/D of JH-*10* is 1.00 higher than 0.98 for FH-*240.* However, the significant D band peaks of FH-*x* and JH-*x* indicate they contain substantial fractions of amorphous carbon. The

presence of amorphous carbon can affect the quantification of G/D ratios based on the two primary peak intensities alone. Thus, we further deconvoluted Raman spectra into five peaks at 1360, 1620, 1520, 1245, and 1580 cm^{-1}, corresponding to D_1, D_2, D_3, D_4, and G bands, respectively (Fig. 4b). D_1, D_2, and D_4 peaks correlate to the disordered graphitic with asymmetrical features, whereas the D_3 peak is associated with amorphous carbon [39-41]. The G/D_3 ratios (calculated based on the intensity of deconvoluted G and D_3 peaks) show similar trends as those of G/D ratios (Table S3-4 in SI). This confirms that the changing trends observed in the G/D ratio originate from the abundances of amorphous and graphitic carbon in FH-*x* and JH-*x*, other than dopings and structural defects in graphitic materials.

Next, we used XPS to analyze the surface chemical composition of the carbon catalysts (Fig. S6 in SI). Fig. 5a shows the representative C 1s spectra of FH-240 and JH-120 with a similar shape. Both are dominated by the C-C bond (284.8 eV) and minor C-O bonds, indicating that most of the H and Zn heteroatoms in ZIF-8 have been removed after the high-temperature thermal treatments in the inert gas environment. However, significant amounts of N are retained in carbon catalysts. Fig. 5b displays the representative N 1s spectra from FH-240 and JH-120. We further deconvoluted the N peaks into 4 peaks at 398.6, 399.8, 401.0, and 403.8 eV, corresponding to pyridinic N, pyrrolic N, graphitic N, and oxidized N, respectively (Table S5-6 in SI). The abundances of total N and the three dominant types of N species (absolute and relative abundances) were quantified, and the results are shown in Fig. 5c against their graphitization time at 900 °C.

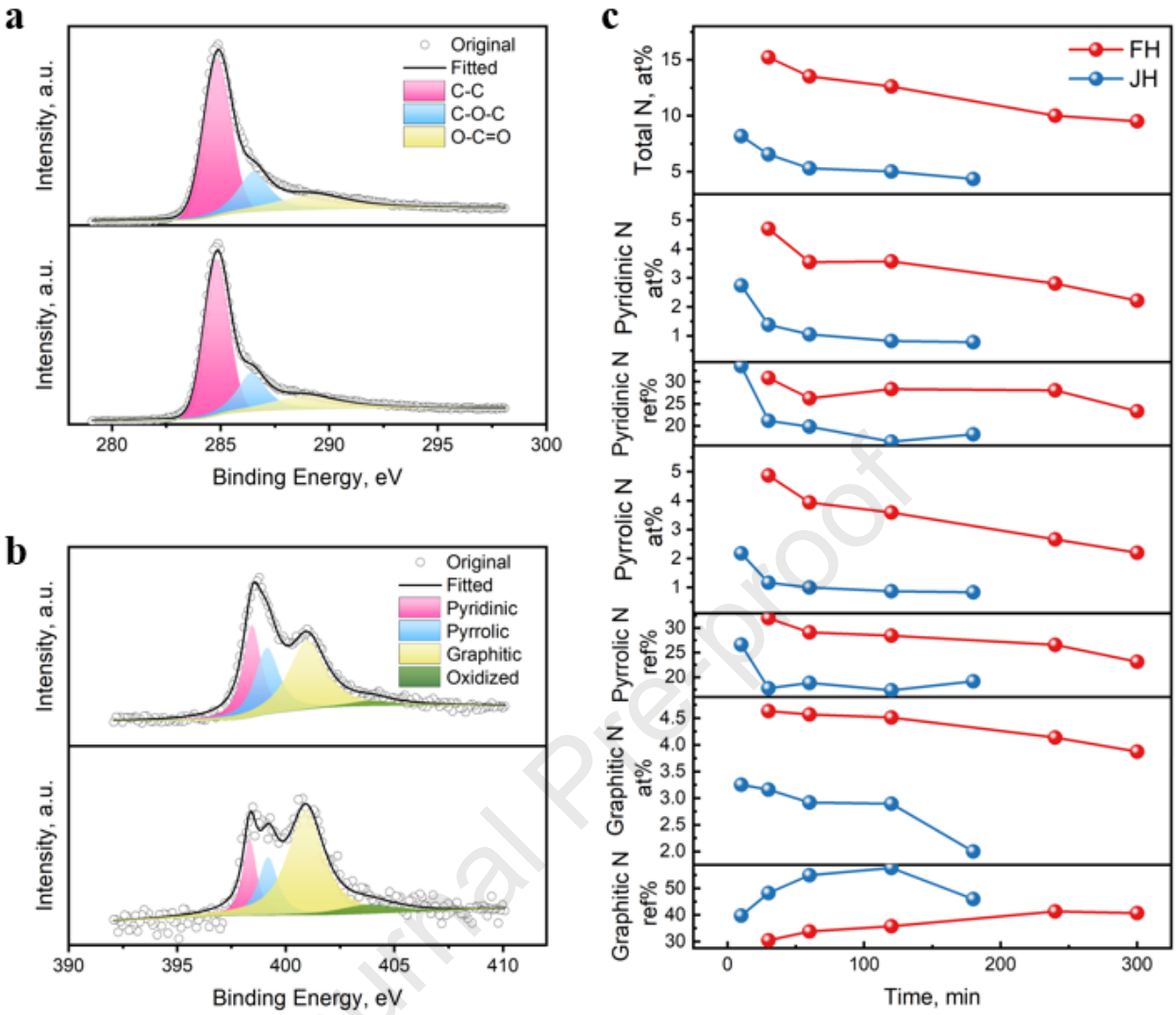

Fig. 5. XPS spectra of carbon catalysts. (a) Deconvoluted XPS C1s spectra of FH-240 and JH-120, (b) deconvoluted XPS N1s spectra of FH-240 and JH-120, (c) the atomic ratio of different N species in carbon catalysts determined from XPS plotted against their graphitization time at 900 °C.

Several interesting trends are observed. First, the total N abundance in FH-*x* is about double that in JH-*x*. For example, FH-240 contains 10.01% N, while JH-120 only has 5.02% N, consistent with the EDX results in Fig. 2b. This indicates that the JH method is more effective in removing heteroatoms. Second, the total N abundance in FH-*x* continuously decreases from 15.22 to 9.51% with the extension of graphitization time from 30 to 300 min. In comparison, the total N abundance in JH-*x* decreases

from 8.18 to 5.31 in 60 min and then becomes more stable and only drops to 4.35% after 180 min. This indicates that the removal of N heteroatoms is almost completed after 60 min in the JH method, while the N removal process continues over 300 min in the FH method. Third, the removals of different types of N species also proceed at different rates. Pyridinic and pyrrolic N abundances decrease sharply in the first 60 min in both methods. In particular, in the JH method, their abundances are around 1% in 60 min and have minor changes afterward. The changes in graphitic N abundance are more stable in the first 120 min. The graphitic N abundance in JH-*x* decreases from 3.3 to 2.9%, then drops to 2.0% in the last 60 min. The graphitic N abundance in FH-*x* reduces from 4.6% to 4.1% in the first 240 min and further lowers to 3.9% at 300 min. When comparing the relative abundance of different N species, the various types of N species distributed evenly in FH-30 and JH-10 with a short graphitization time; pyridinic, pyrrolic, and graphitic N each contributes to about 30% of the total N abundance. However, with the extension of graphitization time, the pyridinic and pyrrolic N in JH-*x* almost diminished after 30–60 min, and graphitic N became the dominant N species. The relative abundance of graphitic N in JH-*x* increased from 39.77 to 57.70% and dropped back to 45.97% at 180 min. In contrast, the relative abundances of pyridinic and pyrrolic N in FH-*x* decayed much slower, reduced from 30.87 to 23.31% and 31.99 to 23.13%, respectively. The relative abundance of graphitic N in FH-*x* was thus much lower than that in JH-*x*, increasing from 30.44 to 41.33% before reaching a stable state at 240 min. These results indicate that although less total N is retained in JH-*x*, the JH method has a higher selectivity towards the formation of graphitic N.

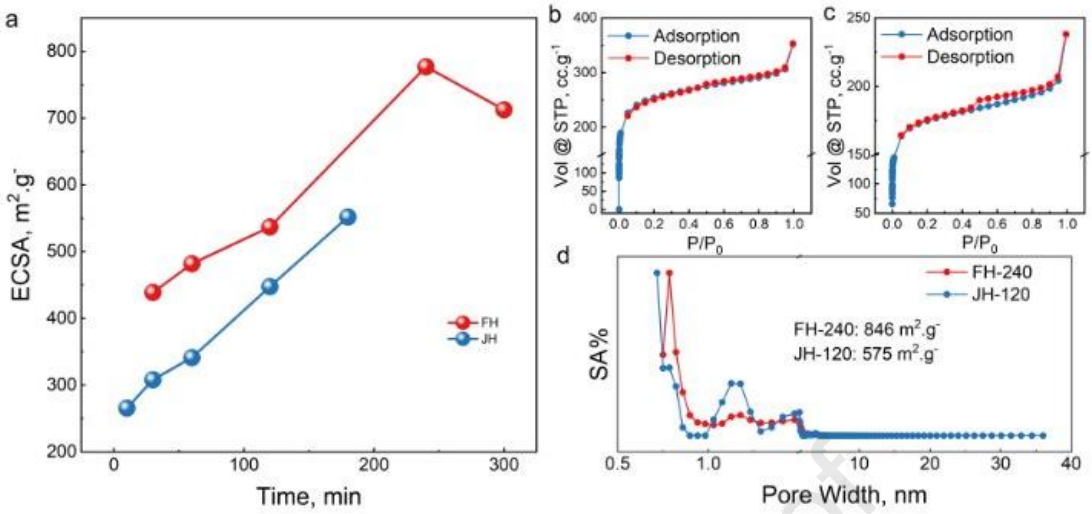

Fig. 6. Surface area analysis of carbon catalysts: (a) ECSA of FH-*x* and JH-*x* against their graphitization time at 900 ºC, N_2 physisorption isotherms of (b) FH-240 and (c) JH-120, (d) pore size distribution of FH-240 and JH-120.

We further examined carbon catalysts' surface area and pore structures by electrochemical and gas adsorption methods. The ECSA of carbon catalysts was determined from their CV scans, as described in the experimental section and shown in Fig. S7–8 in SI. Fig. 6a indicates that the ECSA of FH-*x* and JH-*x* increases with the extension of their graphitization time, except for some decrease of FH-300. FH-*x* has a much larger ECSA than JH-*x*. FH-240 has an ECSA of 776 $m^2\ g^{-1}$, higher than that of JH-120 at 551 $m^2\ g^{-1}$. N_2 physisorption analysis of FH-240 and JH-120 shows similar results. Fig. 6b–c shows their N_2 physisorption isotherms, and the corresponding BET-specific surface area of FH-240 is 846 $m^2\ g^{-1}$ and 575 $m^2\ g^{-1}$ for JH-120. A hysteresis loop was shown in the N_2 physisorption isotherm of JH-120 but was missing in FH-240, as shown in Fig. 2b-c. This is due to the capillary condensation in the presence of mesopores with sizes between 2–50 nm. The presence of mesopores in JH-120 is further confirmed by the pore size distribution analysis conducted using the DFT method. As shown in Fig. 4d, FH-240 contains predominantly micropores with pore size < 2 nm, while JH-120 has increased mesopore contents within the 2–10 nm range. The large specific surface area and pore

structures of ZIF-8-derived carbon materials result from the vicinity and pathways formed during the removal of volatile components in ZIF-8 at the early stage of its pyrolysis, which is influenced by the heating rate [18, 22]. The JH method was about 540 times faster than the FH method. The quicker heating rate may cause faster volatile component removal, resulting in the collapse of small gas pathways but creating more large gas pathways. This explains the observed smaller specific surface area and larger pores in JH-*x*.

However, the above characterization results on the graphitization degree, N heteroatoms, surface area, and pore structures do not correlate straightforwardly with the observed electrochemical properties of carbon catalysts. JH-*x* has a higher degree of graphitization than FH-*x*, but the abundances of their N species are about half of those in FH-*x*. Further, their specific surface is much smaller than that of FH-*x* despite containing some larger pores. Thus, it's crucial to elucidate the interplays among these physiochemical and structural factors and determine which factor plays the most critical role in controlling the electrocatalytic performance of carbon catalysts.

3.5 *An interplay between graphitic N species and graphitization degree of carbon substrates*

We applied Spearman's correlation coefficients to quantitatively analyze which physiochemical and structural properties play the most significant role in the catalytic activity of carbon catalysts for ORR. These properties include G/D, G/D_1, G/D_2, G/D_3, and G/D_4 ratios, the total N abundance, the absolute and relative abundances of pyridinic N, pyrrolic N, and graphitic N, and ECSA. The catalytic activity descriptors include the limiting current (*j*) at 0.1 V and half-wave potential ($E_{Half\text{-}wave}$) (Table S7, SI). Fig. 7a shows that G/D, G/D_1, and G/D_3 ratios all positively correlate with the catalytic performance, indicating that the properties of carbon substrates strongly influence the catalytic activity of carbon catalysts. Among all G/D ratios analyzed, the G/D_3 ratio provides direct information on the relative ratio between graphitic and amorphous carbon content, which also demonstrates the strongest correlation to both performance descriptors, suggesting that higher graphitization degree of carbon

substrate is crucial to achieve improved ORR activity. Higher graphitization favors the formation of graphitic-N over other forms of N coordination, resulting in a higher relative graphitic-N level, as indicated in Fig. S9 in SI. The relative abundance of graphitic N has the highest correlation coefficient with the two catalytic activity descriptors, which suggests that graphitic N species are closely related to catalytic active sites in the carbon catalysts. Notably, the absolute and relative abundances of pyridinic N and pyrrolic N and the total N abundance negatively correlate with catalytic activity. Further, the absolute abundance of graphitic N is negatively correlated with the two catalytic activity descriptors, which suggests that the absolute numbers of graphitic N species do not play a key role. Although ECSA has small positive correlation coefficients (less than 0.5) with the two catalytic activity descriptors, suggesting that the specific surface area of carbon catalysts does not play the most critical role.

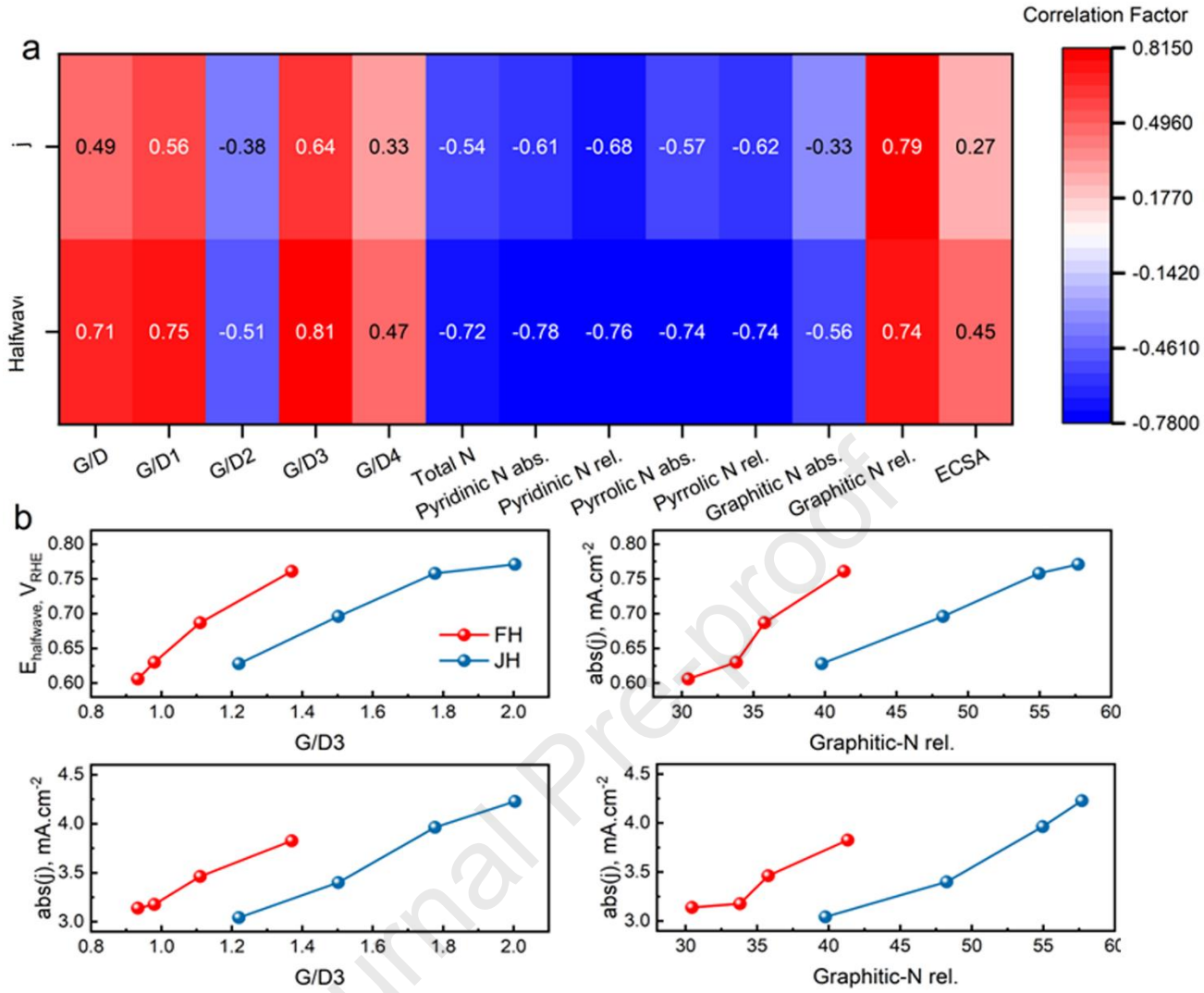

Fig. 7. (a) Spearman's correlation coefficient analysis between physiochemical and structural properties and catalytic activity descriptors of carbon catalysts. (b) The correlations between the two most critical physiochemical and structural properties (G/D_3 ratio and the relative abundance of graphitic N) and the catalytic descriptors (the limiting current (j) at 0.1 V and half-wave potential ($E_{Half\text{-}wave}$)) of carbon catalysts.

We plotted the two physiochemical and structural properties with the highest correlation coefficients (G/D_3, the relative abundance of graphitic N) against the two catalytic activity descriptors, as shown in Fig. 7b. They show a close to linear correlation to catalytic activity. However, the ranges of the two

properties covering FH-*x* and JH-*x* differ. The G/D_3 ratios of JH-*x* increase from 1.22 (JH-10) to 2.00 (JH-120), covering a much broader range than those of the FH-*x*, which only vary by less than 0.1. This suggests that the graphitization degree is unlikely to be the only cause of the difference in their catalytic activity. On the contrary, the relative abundance of graphitic N changes significantly for FH-*x* and JH-*x* and appears to parallel that of both catalytic activity descriptors. Based on these results, we hypothesize that graphitic-N species directly correlate with active catalytic sites in the carbon catalysts. However, the graphitic N species' local structural/chemical environment can significantly influence the catalytic activity, which is controlled by the graphitization degree of carbon substrates.

Next, the turnover frequency (TOF) of catalytic active sites in FH-*x* and JH-*x* was calculated over the 0.7–0.85 V_{RHE} range. Based on the correlation study above, we assumed that three carbon atoms directly bonded to a graphitic N acted as the active sites for ORR. As shown in Fig. 8 a–b, the TOF of FH-*x* and JH-*x* initially increases with the heating period, up to 120 and 240 min, respectively, indicating enhancement to the intrinsic activity of individual active sites. After passing critical heating durations (i.e., 120 min for JH-*x* and 240 min for FH-x), TOF decreased, suggesting excessive heating, resulting in active site deactivation. Fig. 8c shows that JH-*x* has significantly higher TOFs than FH-*x*, with JH-120 having a peak value of 0.023 s^{-1}, more than twice that of the optimal FH-*x* (i.e., FH-240) with a TOF of 0.009 s^{-1}. A higher TOF value indicates the higher intrinsic activity of individual active sites. Thus, the TOF analysis suggests that JH-*x* has significantly higher intrinsic activity than FH-*x*. The activity of a catalyst depends on both the density and intrinsic activity of its active sites. Since carbon atoms next to graphitic-N are regarded as the active sites within the carbon catalysts and from the XPS analysis, we demonstrated that JH-*x* contains fewer graphitic-N (absolute level) compared to FH-*x*, which suggests that JH-*x* has lower active site density than FH-*x*. For instance, JH-120 has a graphitic N abundance of 2.90 wt%, whereas FH-240 has a graphitic N abundance of 4.14 wt%. Thus, we propose that the improved ORR performance of JH-*x* results from their significantly improved intrinsic activity per active site, which outweighed the drawback of their lower active site density. One

key aspect of the structural difference between JH-*x* and FH-*x* is their graphitization degree, which also strongly correlates to the performance trend. This suggests that the active sites' intrinsic activity strongly depends on the graphitization degree of its corresponding carbon substrate, and a higher degree of graphitization benefits the active site's intrinsic ORR activity.

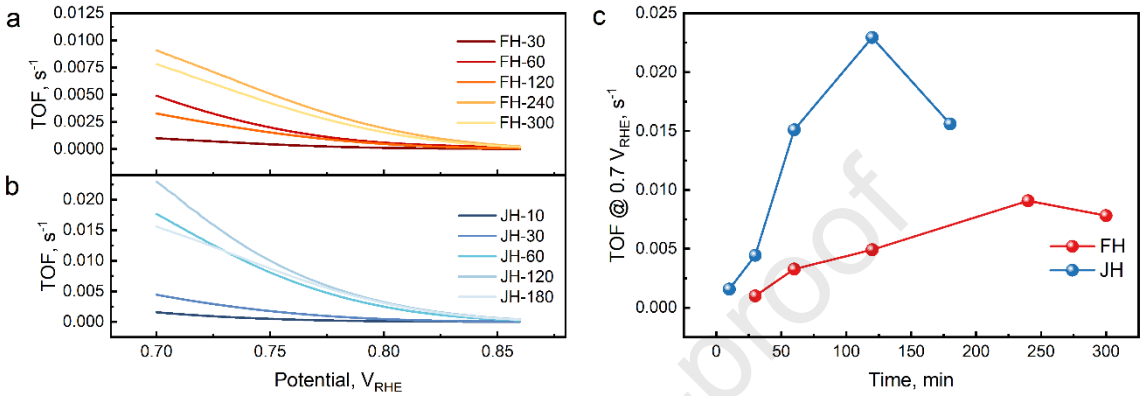

Fig. 8. TOF of catalytically active sites in carbon catalysts. (a) TOF of FH-*x* carbon catalysts over the voltage range of 0.70–0.85 V_{RHE}. (b) TOF of JH-*x* carbon catalysts over the voltage range of 0.70–0.85 V_{RHE}. (c) Comparison of TOFs of carbon catalysts at 0.70 V_{RHE}.

3.6 *Theoretical modeling of catalytically active sites*

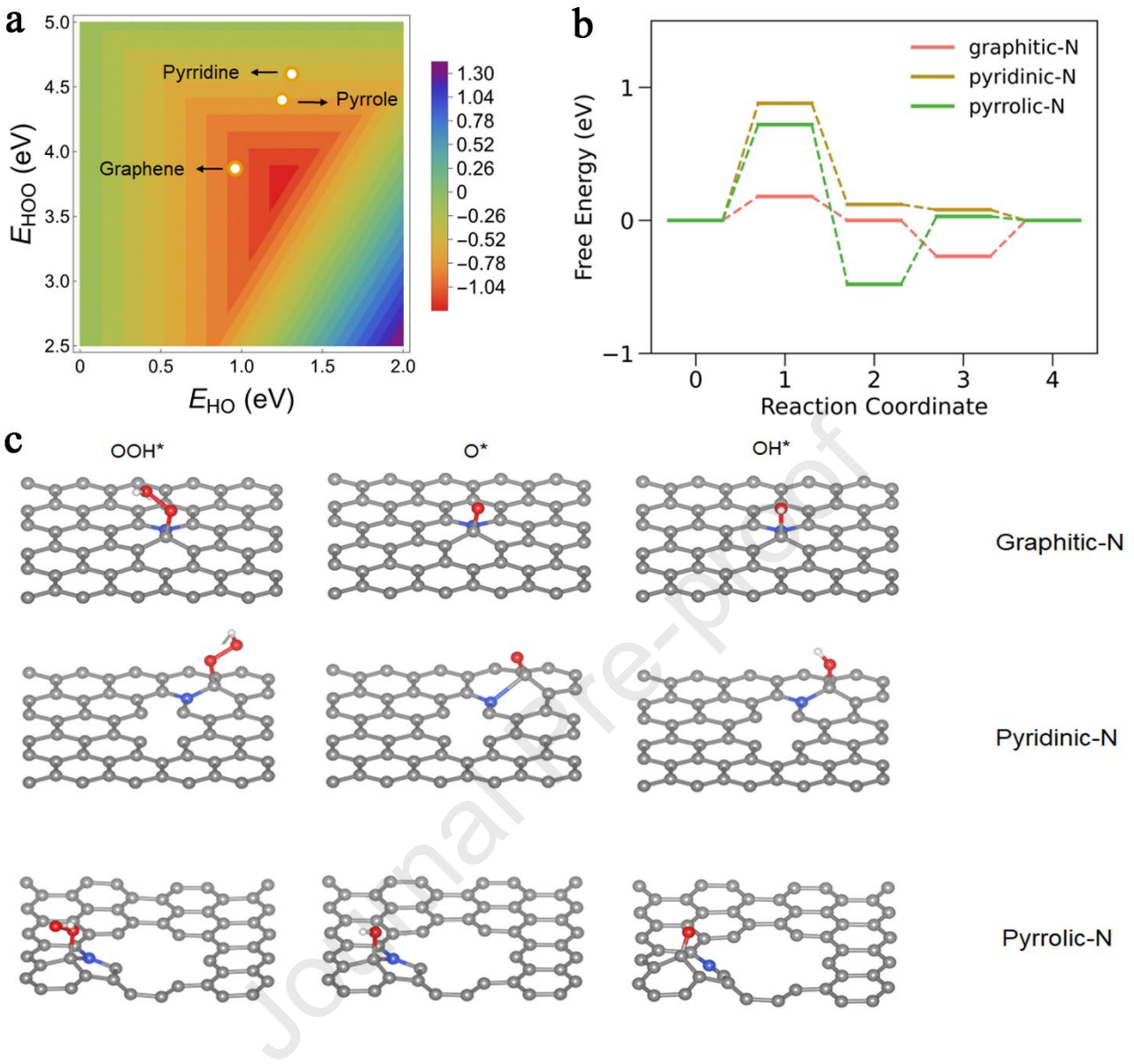

Fig. 9. (a) A volcano map of adsorption energy of ORR reaction intermediates on carbon active sites bonded to different N species. (b) The step-by-step 4-electron ORR free energy diagram for carbon active sites bonded to different N species. (c) Atomic models of the chemisorption of key ORR reaction intermediates on carbon active sites bonded to different N species.

We used theoretical modeling to verify experimental findings further. We constructed several carbon catalyst models by embedding graphitic, pyridinic, and pyrrolic N (blue atoms) in graphene nanosheets (**Fig. 9**c). Three carbon atoms bonded to an N atom were considered catalytically active sites. The

different N species result in different defect densities in graphene nanosheets. Fig. 9c shows that the model containing graphitic N has a higher graphitization level (fewer defects) than those containing pyridinic and pyrrolic N. Then, we calculated the adsorption energy of several key ORR intermediates on these sites. A volcano map of E_{Onset} as a function of the adsorption energy of OH* and OOH* is shown in Fig. 9a. Active sites located near the upper right corner of the volcano diagram suffer from weak *OOH adsorption to initiate ORR, while the difficulty of *OH desorption hinders the ones close to the lower left corner due to the overly strong adsorption of the intermediates. The active site with the optimal 4-electron ORR performance is expected to be found near the center of the volcano map, representing balanced adsorption and desorption energy for different reaction intermediates. Fig. 9a shows that carbon active sites bonded to graphitic N reside closest to the volcano diagram's apex, indicating the highest intrinsic catalytic activity. To elaborate on our findings, we conducted further DFT calculations to identify and compare the different active sites' rate-determining steps (RDS). The RDS is the reaction step associated with the highest free energy change (ΔG) barrier. From the step-by-step free energy diagram in Fig. 9b, the RDS for the active sites bonded to pyridinic and pyrrolic N in more defective graphene models is the transformation of OO* to HOO*, with ΔG values of 0.87 and 0.72 eV, respectively. In contrast, the RDS for the active sites bonded to graphitic N is the conversion of OH* to H_2O with a significantly lower ΔG value of 0.27 eV, leading to its improved 4-electron ORR performance. We also computed the 4-electron ORR activity of defect-free graphitic carbon (a graphene nanosheet), in which case the free energy calculation suggested that the energy barrier is too steep to initiate the OOH* chemisorption onto the catalyst, leading to poor ORR performance (Fig. S10 in SI).

We want to highlight that the findings in the study are relevant to carbon catalysts derived from organic precursors, which have many more defects than those derived from graphitic carbon materials, such as HOPG, CNTs, and pristine graphene. Since graphitic carbon materials are already highly graphitized, the density of dopants or defects that introduce charged atomic sites to carbon materials

interrupt their uniform electron distribution would be the most critical factor in determining their catalytic activity. The more introduced charged atomic sites often increase the overall catalytic activity due to the increased density of catalytic active sites. In contrast, our findings show that the graphitization level of carbon substrates is equally essential for carbon catalysts containing a high density of defects. The intrinsic activity of catalytic active sites in defective carbon substrates is much lower than in more graphitized carbon substrates. A higher density of active sites in defective carbon substrates does not always translate into a higher overall catalytic activity. Balancing the density of active sites and their intrinsic activity via improving the graphitization of carbon substrates is critical to yielding high-performance carbon catalysts.

3.7 *Catalytic performance evaluation in a practical application*

Primary ZABs were assembled to evaluate the practical applicability of the carbon catalysts synthesized in this study. The ZAB assembled using JH-120 showed higher OCP (1.44 vs. 1.36 V), higher maximum power density (143 vs. 123 mW cm^{-2}), and higher specific discharge capacitance (752 vs. 635 mAh g^{-1}) than that assembled using FH-240. Further, ZABs assembled using both FH-240 and JH-120 showed good stability when discharging under varied discharge current densities (Fig. 11 in SI). These carbon catalysts have sufficient catalytic activity for the practical ORR application; specifically, JH-120 enables better performance in ZABs than FH-240, consistent with other characterization results.

4. Conclusion

We synthesized carbon catalysts by carbonizing ZIF-8 at 900 ºC using JH and FH methods over different durations. JH-derived carbon catalysts demonstrate better catalytic activity for 4-electron transfer ORR than FH-derived carbon catalysts. In particular, the optimal JH-120 among JH-derived carbon catalysts has a j of -4.227 mA cm^{-2}, $FE_{H_2O_2}$ of 14.6%, and the Tafel slope of 56 mV dec^{-1},

significantly outperforming the optimal FH-240 among FH-derived carbon catalysts at -3.826 mA cm^{-2}, 19.3% and 58 mV dec^{-1}, respectively. Detailed structural characterization results show that JH-*x* has a higher degree of graphitization than FH-*x*. Still, the abundance of their N species is much lower than that of FH-*x*. Further, JH-*x*'s specific surface is smaller than that of FH-*x* despite containing some larger pores. These structural properties cannot be directly correlated with their catalytic activity. Spearman's correlation coefficient analysis between the physiochemical and structural properties (G/D, G/D_1, G/D_2, G/D_3, and G/D_4 ratios, the total N abundance, the absolute and relative abundances of pyridinic N, pyrrolic N, and graphitic N, and ECSA) and the catalytic activity (*j* and $E_{Half\text{-}wave}$) indicates that catalytically active sites correlate with the relative abundance of graphitic N species, which is further influenced by the graphitization degree of carbon substrates. The TOF of JH-120 with a higher degree of graphitization is 0.023 s^{-1}, more than that of FH-240 with a lower degree of graphitization at 0.009 s^{-1}. The enhanced intrinsic activity of active sites in JH-*x* outpaces their reduced number (due to lower N concentration), contributing to their better catalytic activity. DFT calculation confirms that carbon atoms bonded graphitic N within carbon substrates having a higher graphitization level (fewer defects) have the optimal catalytic activity for 4-electron ORR. The RDS at these sites is the conversion of OH* to H_2O with a significantly lower ΔG value of 0.47 eV compared to other sites in more defective carbon substrates. These experimental and theoretical calculation results provided new insights into carbon catalysts' structural and catalytic activity. Tailoring organic precursors' carbonization conditions to balance the heteroatom coordination environment and carbon substrates' graphitization degree is critical to yield high-performance carbon catalysts. Joule heating offers a valuable approach to regulating such balance.

Declaration of competing interest

The authors declare that they have no known competing financial interests or personal relationships that could have appeared to influence the work reported in this paper.

Acknowledgments

This research was conducted by the ARC Centre of Excellence for Green Electrochemical Transformation of Carbon Dioxide (CE230100017) and funded by the Australian Government. The authors also acknowledge the support from the Australian Research Council under the Discovery Project (DP230101694) and the Future Fellowship (FT210100218), the Japan Society for the Promotion of Science KAKENHI (JP23K13703), the Hirose Foundation, and The University of Sydney under the External Research Collaboration Seed Funding (G221867). HL and LW also acknowledge the Center for Computational Materials Science, Institute for Materials Research, Tohoku University for the use of MASAMUNE-IMR (No. 202212-SCKXX-0204), the Institute for Solid State Physics at the University of Tokyo, the Sydney Info Hub at the University of Sydney, and the National Computational Infrastructure (NCMAS-2024-59) for the computational resources.

Appendix A. Supplementary data

Supplementary data to this article can be found online at

References

[1] L.R. Radovic, F. Rodriguez-Reinoso, Carbon materials in catalysis, Chemistry & Physics of Carbon, CRC Press1996, pp. 261-376.

[2] E. Auer, A. Freund, J. Pietsch, T. Tacke, Carbons as supports for industrial precious metal catalysts, Appl. Catal., A 173(2) (1998) 259-271.

[3] E. Antolini, Carbon supports for low-temperature fuel cell catalysts, Appl. Catal., B 88(1-2) (2009) 1-24.

[4] E. Lam, J.H. Luong, Carbon materials as catalyst supports and catalysts in the transformation of biomass to fuels and chemicals, ACS Catal. 4(10) (2014) 3393-3410.

[5] I.M. Groot, Investigation of active catalysts at work, Acc. Chem. Res. 54(23) (2021) 4334-4341.

[6] K. Gong, F. Du, Z. Xia, M. Durstock, L. Dai, Nitrogen-doped carbon nanotube arrays with high electrocatalytic activity for oxygen reduction, Science 323(5915) (2009) 760-764.

[7] C. Hu, R. Paul, Q. Dai, L. Dai, Carbon-based metal-free electrocatalysts: from oxygen reduction to multifunctional electrocatalysis, Chem. Soc. Rev. 50(21) (2021) 11785-11843.

[8] C.-X. Zhao, J.-N. Liu, J. Wang, D. Ren, B.-Q. Li, Q. Zhang, Recent advances of noble-metal-free bifunctional oxygen reduction and evolution electrocatalysts, Chem. Soc. Rev. 50(13) (2021) 7745-7778.

[9] P. Cui, L. Zhao, Y. Long, L. Dai, C. Hu, Carbon-based electrocatalysts for acidic oxygen reduction reaction, Angew. Chem. Int. Ed. 62(14) (2023) e202218269.

[10] D. Guo, R. Shibuya, C. Akiba, S. Saji, T. Kondo, J. Nakamura, Active sites of nitrogen-doped carbon materials for oxygen reduction reaction clarified using model catalysts, Science 351(6271) (2016) 361-365.

[11] T. Xing, Y. Zheng, L.H. Li, B.C. Cowie, D. Gunzelmann, S.Z. Qiao, S. Huang, Y. Chen, Observation of active sites for oxygen reduction reaction on nitrogen-doped multilayer graphene, ACS Nano 8(7) (2014) 6856-6862.

[12] H. Zhao, C. Sun, Z. Jin, D.-W. Wang, X. Yan, Z. Chen, G. Zhu, X. Yao, Carbon for the oxygen reduction reaction: A defect mechanism, J. Mater. Chem. A 3(22) (2015) 11736-11739.

[13] Y. Jia, L. Zhang, A. Du, G. Gao, J. Chen, X. Yan, C.L. Brown, X. Yao, Defect graphene as a trifunctional catalyst for electrochemical reactions, Adv. Mater. 28(43) (2016) 9532-9538.

[14] S. Xu, A. Dong, Y. Hu, Z. Yang, S. Huang, J. Qian, Multidimensional MOF-derived carbon nanomaterials for multifunctional applications, J. Mater. Chem. A 11(18) (2023) 9721-9747.

[15] L. Zhang, Z. Su, F. Jiang, L. Yang, J. Qian, Y. Zhou, W. Li, M. Hong, Highly graphitized nitrogen-doped porous carbon nanopolyhedra derived from ZIF-8 nanocrystals as efficient electrocatalysts for oxygen reduction reactions, Nanoscale 6(12) (2014) 6590-6602.

[16] X. Wang, H. Zhu, C. Yang, J. Lu, L. Zheng, H.-P. Liang, Mesoporous carbon promoting the efficiency and stability of single atomic electrocatalysts for oxygen reduction reaction, Carbon 191 (2022) 393-402.

[17] Y. Wu, J. Liu, Q. Sun, J. Chen, X. Zhu, R. Abazari, J. Qian, Molecular catalyst of Fe phthalocyanine loaded into In-based MOF-derived defective carbon nanoflowers for oxygen reduction, Chem. Eng. J. 483 (2024) 149243.

[18] N. Cui, K. Bi, W. Sun, Q. Wu, Y. Li, T. Xu, B. Lv, S. Zhang, Effect of pyrolysis conditions on the performance of Co–doped MOF–derived carbon catalysts for oxygen reduction reaction, Catalysts 11(10) (2021) 1163.

[19] T. Jiang, W. Jiang, Y. Li, Y. Xu, M. Zhao, M. Deng, Y. Wang, Facile regulation of porous N-doped carbon-based catalysts from covalent organic frameworks nanospheres for highly-efficient oxygen reduction reaction, Carbon 180 (2021) 92-100.

[20] M. Liu, X. Zhu, Y. Song, G. Huang, J. Wei, X. Song, Q. Xiao, T. Zhao, W. Jiang, X. Li, Bifunctional edge-rich nitrogen doped porous carbon for activating oxygen and sulfur, Adv. Funct. Mater. 33(11) (2023) 2213395.

[21] Y. Chen, Y. Huang, M. Xu, T. Asset, X. Yan, K. Artyushkova, M. Kodali, E. Murphy, A. Ly, X. Pan, Catalysts by pyrolysis: Direct observation of transformations during re-pyrolysis of transition metal-nitrogen-carbon materials leading to state-of-the-art platinum group metal-free electrocatalyst, Mater. Today 53 (2022) 58-70.

[22] Y. Huang, Y. Chen, M. Xu, T. Asset, P. Tieu, A. Gili, D. Kulkarni, V. De Andrade, F. De Carlo, H.S. Barnard, Catalysts by pyrolysis: Direct observation of chemical and morphological transformations leading to transition metal-nitrogen-carbon materials, Mater. Today 47 (2021) 53-68.

[23] Y. Zeng, C. Li, B. Li, J. Liang, M.J. Zachman, D.A. Cullen, R.P. Hermann, E.E. Alp, B. Lavina, S. Karakalos, Tuning the thermal activation atmosphere breaks the activity–stability trade-off of Fe–N–C oxygen reduction fuel cell catalysts, Nat. Catal. 6(12) (2023) 1215-1227.

[24] V. Armel, J. Hannauer, F. Jaouen, Effect of zif-8 crystal size on the O2 electro-reduction performance of pyrolyzed Fe–N–C catalysts, Catalysts 5(3) (2015) 1333-1351.

[25] J. Zou, X. Zhang, C. Xu, J. Zhao, Y.T. Zhu, Q. Li, Soldering carbon nanotube fibers by targeted electrothermal-induced carbon deposition, Carbon 121 (2017) 242-247.

[26] H. Huang, S. Zhou, C. Yu, H. Huang, J. Zhao, L. Dai, J. Qiu, Rapid and energy-efficient microwave pyrolysis for high-yield production of highly-active bifunctional electrocatalysts for water splitting, Energy Environ. Sci. 13(2) (2020) 545-553.

[27] J. Zou, H. Dong, H. Wu, J. Huang, X. Zeng, Y. Dou, Y. Yao, Z. Li, Laser-induced rapid construction of Co/N-doped honeycomb-like carbon networks as oxygen electrocatalyst used in zinc-air batteries, Carbon 200 (2022) 462-471.

[28] J.P. Perdew, K. Burke, M. Ernzerhof, Generalized gradient approximation made simple, Phys. Rev. Lett. 77(18) (1996) 3865-3868.

[29] G. Kresse, J. Furthmüller, Efficient iterative schemes for ab initio total-energy calculations using a plane-wave basis set, Phy. Rev. B 54(16) (1996) 11169-11186.

[30] W. Kohn, L.J. Sham, Self-consistent equations including exchange and correlation effects, Phys. Rev. 140(4A) (1965) A1133-A1138.

[31] P.E. Blöchl, Projector augmented-wave method, Phys. Rev. B 50(24) (1994) 17953-17979.

[32] C. Liu, H. Li, F. Liu, J. Chen, Z. Yu, Z. Yuan, C. Wang, H. Zheng, G. Henkelman, L. Wei, Y. Chen, Intrinsic activity of metal centers in metal–nitrogen–carbon single-atom catalysts for hydrogen peroxide synthesis, J. Am. Chem. Soc. 142(52) (2020) 21861-21871.

[33] J.K. Nørskov, J. Rossmeisl, A. Logadottir, L. Lindqvist, J.R. Kitchin, T. Bligaard, H. Jónsson, Origin of the overpotential for oxygen reduction at a fuel-cell cathode, J. Phys. Chem. B 108(46) (2004) 17886-17892.

[34] J.B. James, Y.S. Lin, Kinetics of ZIF-8 thermal decomposition in inert, oxidizing, and reducing environments, J. Phys. Chem. C 120(26) (2016) 14015-14026.

[35] Y. Deng, Y. Dong, G. Wang, K. Sun, X. Shi, L. Zheng, X. Li, S. Liao, Well-defined ZIF-derived Fe–N codoped carbon nanoframes as efficient oxygen reduction catalysts, ACS Appl. Mater. Interfaces 9(11) (2017) 9699-9709.

[36] B. Lü, W. Qi, M. Luo, Q. Liu, L. Guo, Fischer–Tropsch synthesis: ZIF-8@ ZIF-67-Derived cobalt nanoparticle-embedded nanocage catalysts, Ind. Eng. Chem. Res. 59(27) (2020) 12352-12359.

[37] S. Wei, Y. Sun, Y.-Z. Qiu, A. Li, C.-Y. Chiang, H. Xiao, J. Qian, Y. Li, Self-carbon-thermal-reduction strategy for boosting the Fenton-like activity of single Fe-N4 sites by carbon-defect engineering, Nat. Commun. 14(1) (2023) 7549.

[38] A.C. Ferrari, J. Robertson, Interpretation of Raman spectra of disordered and amorphous carbon, Phys. Rev. B: Condens. Matter 61(20) (2000) 14095.

[39] A. Sadezky, H. Muckenhuber, H. Grothe, R. Niessner, U. Pöschl, Raman microspectroscopy of soot and related carbonaceous materials: Spectral analysis and structural information, Carbon 43(8) (2005) 1731-1742.

[40] Y. Kouketsu, T. Mizukami, H. Mori, S. Endo, M. Aoya, H. Hara, D. Nakamura, S. Wallis, A new approach to develop the Raman carbonaceous material geothermometer for low-grade metamorphism using peak width, Isl. Arc 23(1) (2014) 33-50.

[41] C.C. Zhang, S. Hartlaub, I. Petrovic, B. Yilmaz, Raman spectroscopy characterization of amorphous coke generated in industrial processes, ACS Omega 7(3) (2022) 2565-2570.

Declaration of interests

☒ The authors declare that they have no known competing financial interests or personal relationships that could have appeared to influence the work reported in this paper.

☐ The authors declare the following financial interests/personal relationships which may be considered as potential competing interests: